Bi-exponential proton transverse relaxation rate (R_2) image analysis using RF field intensity-weighted spin density projection: potential for R_2 measurement of iron-loaded liver

Paul R. Clark, Wanida Chua-anusorn, Timothy G. St. Pierre*

School of Physics, The University of Western Australia, Crawley, Perth, Western Australia 6009, Australia

Abstract

A bi-exponential proton transverse relaxation rate (R_2) image analysis technique has been developed that enables the discrimination of dual compartment transverse relaxation behavior in systems with rapid transverse relaxation enhancement. The technique is particularly well suited to single spin-echo imaging studies where a limited number of images are available for analysis. The bi-exponential R_2 image analysis is facilitated by estimation of the initial proton spin density signal within the region of interest weighted by the RF field intensities. The RF field intensity-weighted spin density map is computed by solving a boundary value problem presented by a high spin density, long T_2 material encompassing the region for analysis. The accuracy of the bi-exponential R_2 image analysis technique is demonstrated on a simulated dual compartment manganese chloride phantom system with relaxation rates and relative population densities between the two compartments similar to the bi-exponential transverse relaxation behavior expected of iron loaded liver. Results from analysis of the phantoms illustrate the potential of bi-exponential R_2 image analysis with RF field intensity-weighted spin density projection for quantifying transverse relaxation enhancement as it occurs in liver iron overload. © 2003 Elsevier Inc. All rights reserved.

Keywords: MRI; R_2; Liver; Iron; Bi-exponential

1. Introduction

Magnetic resonance imaging methods for the non-invasive measurement of liver iron concentration have focused primarily on quantifying the proton transverse relaxation enhancement caused by biogenic iron oxide deposits within the liver. The intent behind these studies is to determine a calibration curve that relates the reduction in hydrogen proton signal intensity within the liver with the liver iron concentration, either through the liver signal intensity from a single image [1,2], or from the liver transverse relaxation rate (R_2) calculated from multiple spin-echo images [3–5]. Of these two approaches, signal intensity ratio (SIR) methods are inherently less sensitive than relaxation rate methods, as the SIR is effectively calculated for a single point in time on the transverse magnetisation decay curve.

The factors affecting the accuracy, sensitivity, and dynamic range of transverse relaxation rate measurements are the spin-echo measurement times at which the images are acquired, the volume of the liver over which the relaxation rates are calculated, the measured signal intensity, and the image processing scheme used to model the signal decay. Where the spin-echo times are too long to enable the measurement of sufficient signal intensity for the accurate calculation of transverse relaxation times, no correlation with liver iron concentration has been found [6,7]. However, for shortened image acquisition times, a significant correlation between R_2 ($1/T_2$) and liver biopsy iron concentration has been observed [3–5]. The dynamic range for the quantification of liver iron levels is further improved by magnetic resonance spectroscopy (MRS) techniques [8,9]. However, MRS techniques sacrifice imaging capability for the improved signal-to-noise ratio (SNR) of measuring a single enlarged volume element at shorter echo times. Consequently, localized volume spectroscopy provides only a single value for the liver iron concentration throughout the measurement volume. R_2 imaging of the liver, on the other hand, yields information on the variation in iron concentra-

* Corresponding author. Tel.: +618-9380-2747; fax: +618-9380-1014.

E-mail address: stpierre@physics.uwa.edu.au (T.G. St. Pierre).

tion throughout the liver, enabling both the average iron concentration to be calculated and the variation in iron concentration to be imaged [10,11].

A limitation of the former transverse relaxation rate measurement techniques [3–5,8–10] is that they all employ mono-exponential analysis for determination of the transverse relaxation processes within the liver. However, given the anatomic and chemical compartmentalisation of the body's hydrogen protons [12,13], multi-exponential transverse relaxation is expected of the various organs and tissues of the body. For hereditary hemochromatosis patients, MRS measurements [14] have shown that transverse relaxation processes within iron loaded liver are at least bi-exponential in nature.

To improve the diagnostic capability of R_2 measurements of the liver, particularly in relation to the measurement of liver iron overload, the move to bi-exponential analysis of transverse relaxation processes is warranted. Further, to enable accurate bi-exponential transverse relaxation rate analysis across multiple MR platforms, the analysis technique must accommodate both instrument and patient dependencies. The key factors to be taken into account are:

  i) The change or drift in imaging gain between successive spin-echo measurements.
 ii) The effects of thermal and structured noise originating from both the instrument and patient on the non-zero baseline noise distribution of the magnitude image data.
iii) The noise filtering necessary for accurate determination of the relaxation parameters.
iv) The curve fitting procedure for calculation of the relaxation parameters where a small data set is available for analysis; $N \approx 2M$, where M is the number of unknown parameters and N is the number of spin-echo images available. A small number of spin-echo images will typically be available for analysis where a single spin-echo imaging methodology is used [3,4,10].

In this paper, an R_2 image analysis technique is presented which enables the discrimination of bi-exponential transverse relaxation processes in systems with rapid transverse relaxation enhancement, where the transverse relaxation times may be shorter than the minimum echo time that can be measured. The R_2 image analysis is facilitated by incorporating an estimate of the initial proton spin density signal within the subject weighted by the spatial variation in RF field intensity. The RF intensity at each point within the region of interest is computed by the solution of a boundary value problem presented by a high spin density, long T_2 material encompassing the region for analysis. To evaluate the precision and accuracy of the R_2 imaging technique on both mono-exponential and bi-exponential transverse relaxation systems, a series of aqueous manganese chloride (MnCl$_2$) phantoms were studied, from which the bi-exponential system was digitally simulated. The relaxation rates and relative population densities of the two compartments in the bi-exponential system were chosen according to the bi-exponential relaxation properties reported for normal and iron-loaded animal liver [15,16].

2. Materials and methods

2.1. Phantom system preparation

The mono-exponential R_2 phantom system consisted of a series of aqueous MnCl$_2$ solutions prepared to concentrations of 0.100, 0.200, 0.300, 0.400, 0.500, 0.600, 0.700, 0.800, 1.000, 1.200, 1.400, 1.600, 1.800, 2.000, 2.400, 2.800 and 3.200 mM. The solutions were imaged in test tubes of 25 mm internal diameter and 25 mL in volume, arranged in alternating high and low concentrations in a cardboard box padded with plastic bags filled with lard. The lard was obtained from commercially extracted pig fat, and served to provide a high spin density, long T_2 boundary material about the phantoms. The signal intensities from the lard boundary enabled the modeling of the effective RF field intensity-weighted hydrogen proton spin density at every point within the lard boundary (see later). A 1000 mL bag of Hartmann's solution (compound sodium lactate, Baxter, Viaflex® (NaCl 6g, sodium lactate 3.22 mg, KCl 400 mg, CaCl$_2$ 270 mg)) was imaged together with the MnCl$_2$ phantoms to provide a reference signal intensity for the correction of instrumental drift.

A bi-exponential R_2 phantom system was generated from the spin-echo image series of the MnCl$_2$ phantoms by re-ordering the position of the phantoms with digital image editing tools in a duplicate set of images, and then adding the reordered phantom images to the original images with a specified weighting. To accommodate the variation in RF field intensity throughout the phantom space, the image intensities of the reordered phantoms were scaled according to the RF field intensity-weighted spin density at the two different phantom positions (see later for details of RF field intensity-weighted spin density projection). The phantoms were reordered such that on addition to the original image, the ratio between the fast and slow relaxation times was approximately 3:1, as has previously been reported for normal rat liver [15]. The relative proton population densities of the fast and slow transverse relaxation components were set at 85% and 15% respectively. This ratio was a compromise between the relative proton population densities of the fast and slow relaxation components reported for normal rat liver of 90% and 10% [15], and the relative amplitude of the fast-decay component reported in the livers of iron loaded marmosets of approximately 80% [16]. The effective MnCl$_2$ concentrations of the dual compartment system were calculated by summation of the separate concentrations weighted by their relative contributions.

2.2. Single spin-echo image acquisition

Magnetic resonance imaging was performed on a 1.5 T whole body scanner (Siemens MAGNETOM Vision Plus) at a temperature of 20°C. A chest coil was used for signal detection. Axial image slices were acquired with a single-spin-echo (SSE) pulse sequence, with a pulse repetition time TR of 2500 ms, spin-echo times TE of 6, 7, 8, 9, 12, 15, and 18 ms, and slice thickness = 20 mm. A half Fourier 192 × 256 image reconstruction matrix was used over a field of view (FOV) of 350 mm, giving a resulting pixel resolution of approximately 1.4 × 1.4 mm. All spin-echo sequences were run under fixed gain control.

2.3. Image pre-processing

2.3.1. External reference correction of gain drift

The Hartmann's solution, which has an extremely long T_2 compared with the echo times of the measurement sequence, and thus negligible decay in signal intensity, was used as an external reference for the correction of instrumental drift. The correction procedure adopted was to use the signal intensity of the Hartmann's solution in the 6 ms spin-echo image as a reference intensity, and to scale the signal intensities in the remaining spin-echo images relative to any change in the Hartmann's solution signal intensity. The scale factors relating the 6 ms spin-echo image intensity to successive spin-echo images were calculated on a voxel by voxel basis for a region of interest (ROI) over the Hartmann's solution excluding image artifacts. The procedure for scaling the spin-echo image intensities to compensate for gain drift is outlined below:

i) smooth the Hartmann's solution signal intensities by spatial neighborhood averaging over a 5 × 5 window kernel in each spin-echo image to reduce noise,
ii) determine the ratios of the voxel intensities in the Hartmann's solution from each spin-echo image to the corresponding voxel intensities in the 6 ms spin-echo image,
iii) calculate the mean voxel intensity ratio for each spin echo image to yield a scale factor of the mean drift in image intensity relative to the 6 ms spin-echo image,
iv) divide the image intensities through by the scale factor for the mean drift in image intensity.

2.3.2. Noise distribution modeling and baseline correction

To model the background noise of the magnitude MR data, a generalized Poisson distribution (GPD) was used which included a dispersive term λ [17], and Stirling's approximation to the factorial in the numerator:

$$p_S(S) = \alpha \frac{\theta(\theta + S\lambda)^{(S-1)}e^{-(\theta + S\lambda)}}{\sqrt{2\pi S}\,(S/e)^S}, \; S \geq 1$$

where S is the measured signal intensity, α is a scale factor,

and θ and λ parameterise the GPD. The mean, μ, of the GPD (which is the signal level offset S_{LO} of the magnitude MR data) is given by

$$\mu = \theta(1 - \lambda)^{-1} = S_{LO}$$

and the variance σ^2 by

$$\sigma^2 = \theta(1 - \lambda)^{-3}.$$

The background noise level may be taken as $\mu + \sigma$. The GPD is appropriate where non-random sources of noise are present in the magnitude MR data, such as ghosting, ringing and nonuniform signal distributions [18], which may lead to over-dispersion of the Rician distributed thermal noise component [19]. The Levenberg-Marquadt method of non-linear regression [20,21] was used to fit the GPD to a region of the background free of obvious image artifacts.

To correctly model the decay in signal intensity over the spin-echo image sequence, the signal level offset for each image must be subtracted from the image before analysis of the signal decay. This offset must be subtracted in quadrature given the complex origin of the MR signal. The corrected signal intensity (S_C) for a given voxel within the magnitude image is given by:

$$S_C^2 = S_M^2 - S_{LO}^2$$

where S_M is a measured signal intensity, S_{LO} is the background signal level offset, and S_C is an estimate for the signal intensity in the absence of noise. When S_M is less than S_{LO}, S_C is set to zero. This signal intensity correction scheme is reported to work well for signal-to-noise ratios (SNRs) greater than 1 [22].

2.3.3. RF field intensity-weighted spin density projection

For axial images acquired with a chest coil, the RF field intensity diminishes from the approximate RF source locations at diagonal positions about the subject toward the central location between the top and bottom arrays. From the lard surrounding the $MnCl_2$ phantoms, the decay profile of the RF field was found to follow that of elliptically radiating point sources positioned at the local maxima in signal intensity at the lard to air boundary. The degree of ellipticity was adjusted to provide the best fit of the signal decay profile to the lard edge intensities, which modeled the effective RF penetration efficiency. An exponential model was used to specify the RF decay profile, with an identical exponent for each source. An initial estimate for the signal decay rate was determined by averaging the decay rate from single exponentials fitted to each maxima and the two closest neighboring minima on the lard boundary. Curve fitting of the signal decay profile to the lard edge intensities was accomplished by a simplex-simulated annealing routine based on the method of Press and Teukolsky [23].

The signal decay profile fitted to the lard boundary in the 6 ms spin-echo image was transformed to the initial signal intensity profile expected within the lard at TE = 0 ms using the transverse relaxation rate measured for the lard. In this

way, the initial signal intensity for every voxel within the field of view can be calculated for the case where the entire volume is occupied by lard. The initial signal intensity for each voxel within the $MnCl_2$ phantoms, $S(0)$, was then calculated by multiplying the estimated initial signal intensity for the lard at each voxel by the spin density ratio of water to lard (see Results section). The estimate of the initial signal intensity for a given voxel within the phantoms was then incorporated into the R_2 image analysis as an additional datum at TE = 0 ms. The percentage uncertainty on the initial signal intensity was set to twice the percentage decay in signal intensity for the lard from TE = 0 ms to TE = 6 ms.

2.4. Proton transverse relaxation analysis

2.4.1. Mono-exponential proton transverse relaxation analysis

The mono-exponential decay in signal intensity for the phantom data was modeled by the expression for the decay in transverse magnetisation following a SSE pulse sequence [24]:

$$S(TE) = S(0)e^{-R_2 \cdot TE}$$

from which the T_1 factor has been omitted given the long repetition time of the measurement sequence. This equation was fitted to the corrected voxel intensity data as a function of the spin-echo time TE by the Levenberg-Marquardt method for non-linear regression, which follows a χ^2 minimization strategy [20,21]. To reduce the erroneous affects of image noise on the voxel by voxel analysis, the image intensities within the region of interest (ROI) were smoothed by spatial neighborhood averaging over a 5×5 window kernel prior to curve fitting. The error bars on the smoothed signal intensities for the curve fitting procedure were determined by computing the standard error on the mean over the 5×5 window kernel on the unsmoothed data. Curve fitting to the signal intensities corrected by quadrature subtraction of the signal level offset was compared to that for image intensity correction with linear subtraction of the signal level offset. The transverse relaxation analysis was also performed with and without spin density projection to determine if there was any systematic error in the spin density projection method.

2.4.2. Bi-exponential proton transverse relaxation analysis

The bi-exponential decay in transverse magnetisation for the dual compartment phantom system was modeled by the expression:

$$S(TE) = S_f(0)e^{-R_{2f} \cdot TE} + S_s(0)e^{-R_{2s} \cdot TE}$$

where $S_f(0)$ is the amplitude of the fast relaxation component and R_{2f} is its transverse relaxation rate, and $S_s(0)$ is the amplitude of the slow relaxation component and R_{2s} is the slow relaxation rate. The average relaxation rate for the dual compartment system is given by:

$$R_2 = \rho_f R_{2f} + \rho_s R_{2s}$$

where

$$\rho_f = \frac{S_f(0)}{S_f(0) + S_s(0)} \text{ and } \rho_s = \frac{S_s(0)}{S_f(0) + S_s(0)}$$

are the relative population densities of the fast and slow relaxation components, respectively.

Curve fitting of the bi-exponential decay model to the corrected voxel intensity data as a function of TE was performed by a simplex-simulated annealing strategy following the method of Press and Teukolsky [23]. A least-pth power formulation [25,26] was used for minimization of the difference between the fitted model and the measured data:

$$\chi^P = \sum_{i=1}^{N} \left(\frac{y_i - y(x_i; a_1 \dots a_M)}{\sigma_i} \right)^P, p \text{ even}$$

where N is the number of data points, y_i is the measured data, $y(x_i; a_1 a_M)$ is the fitted model, M is the number of unknowns to the model, and σ_i is the uncertainty on the measured data. To sufficiently improve convergence to an optimal solution given the small number of data points available for analysis, p was increased from the standard χ-squares minimization value of 2 to 8.

2.5. Statistical analysis

Linear regression fits and correlation coefficients (r) were determined by the method of least squares and Pearson's method. Linear fits for the determination of relaxivity values were constrained to pass through the proton transverse relaxation rate of pure water. A two-sided matched pairs t-test was used to determine whether transverse relaxation rate values calculated via spin density projection were the same as those determined without. A χ-squares (χ^2) test was used to determine the goodness-of-fit in modeling of the data, and an F-test on the reduced χ-squares ratio was used to determine whether one model for a given set of data was better than an alternative model (see the Appendix for details). The criterion for an acceptable fit to the data was $\chi^2 \leq \nu$ ($\nu \leq 30$) [21], where ν is the number of degrees of freedom for the fit.

3. Results

3.1. Image pre-processing

3.1.1. Noise distribution modeling

An example of the underlying noise profile in the spin-echo image data is illustrated in Fig. 1 for a region of the background in the 6 ms spin-echo image that was free of image artifacts. The histogram is fitted with both a Rician and generalized Poisson distribution, for which the respective Pearson correlation coefficients are 0.987 and 0.994.
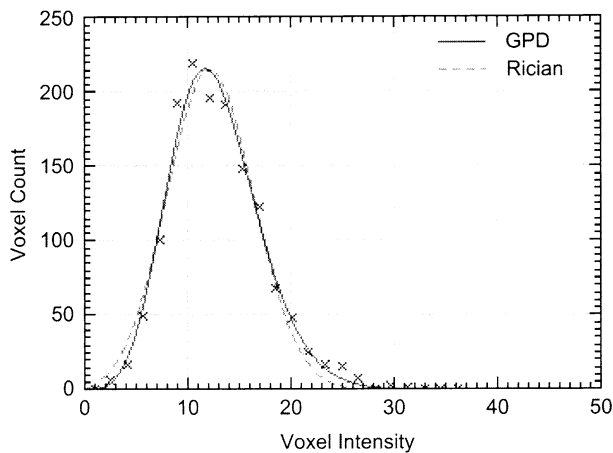
Fig. 1. Distribution of voxel intensities in the 6 ms spin-echo image in a region of the background free of image artifacts. The solid line is the fit of a generalized Poisson distribution ($r = 0.994$), the dashed line the fit of a Rician distribution ($r = 0.987$).

The F -test on the reduced χ-squares ratio of the Rician fit to the noise data relative to the GPD is 2.1, which indicates that the GPD is a better model than the Rician distribution at the significance level $p = 0.05$ ($\nu = 20$). Across the entire set of spin-echo images, the average F value was 2.6, corresponding to a significance level $p < 0.05$. This indicates that the GPD is a statistically better model to the underlying noise distribution of the magnitude image data than the Rician distribution.

3.1.2. Spin density projection

The variation in RF field intensity determined from the lard in the 6 ms spin-echo image is illustrated in Fig. 2a. The image can be thought of as the expected image of a large phantom of lard occupying the entire sample space. The variations in signal intensity in the projected intensity image may be compared with the actual signal intensity variations throughout the lard in the 6 ms spin-echo image in Fig. 2b.

To transform the map of projected signal intensities within the lard to the expected signal intensities within the

$MnCl_2$ phantoms at TE = 0 ms, the map was multiplied by a scale factor incorporating the percentage decay in signal intensity of the lard at TE = 6 ms, and the relative spin density between the aqueous $MnCl_2$ solutions and lard. The relative spin density between aqueous $MnCl_2$ and lard was determined via transverse relaxation rate analysis of the 0.200 mM $MnCl_2$ solution and a neighboring region of lard, which were found to have very similar transverse relaxation rates (18 s^{-1} and 20 s^{-1} respectively). The scale factor relating the spin density of aqueous $MnCl_2$ to lard could thus be simply determined from the ratio in signal intensities of the 0.200 mM $MnCl_2$ solution and the adjacent lard in the 6 ms spin-echo image. The scale factor for the relative spin density was approximately 1.4.

3.2. R_2 image analysis

3.2.1. Homogenous system

The results of the mono-exponential R_2 analyses on the homogeneous $MnCl_2$ phantom system are shown in Fig. 3 with the mean value of R_2 within the phantom, $\langle R_2 \rangle$, plotted versus $MnCl_2$ concentration ($[MnCl_2]$). Linear subtraction of the signal level offset from the magnitude image data shows a significant departure from the expected linear relationship between R_2 and paramagnetic ion concentration in solution. For quadrature subtraction of the signal level offset from the magnitude image data, there was a highly significant linear correlation between $\langle R_2 \rangle$ and $[MnCl_2]$ ($r = 0.99991$). Statistically, there was no significant difference between the R_2 image analysis performed with or without spin density projection (two-sided matched pairs t test). The relaxivity (slope of $\langle R_2 \rangle$ versus $[MnCl_2]$) for the R_2 image analysis performed with spin density projection was 74.3 ± 0.2 s^{-1} mM^{-1}, and was 74.2 ± 0.3 s^{-1} mM^{-1} for the R_2 image analysis performed without spin density projection. The χ^2 probability Q_χ of the goodness-of-fit for monoexponential R_2 image analysis satisfied the criterion of $\chi^2 \leq \nu$ for an acceptable fit to the data for all of the phantoms. R_2 image analysis with spin density projection was better than the analysis without, where the minimum Q_χ was 80%, as
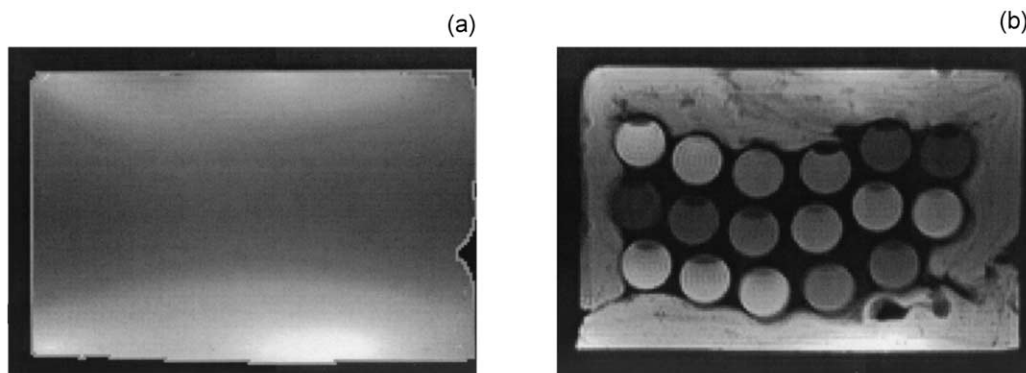

Fig. 2. (a) Image showing the calculated RF field intensity-weighted signal at TE = 6 ms throughout the sample space, if the entire volume was filled with lard. (b) Measured 6 ms spin-echo image of the $MnCl_2$ phantoms and lard for comparison with (a).
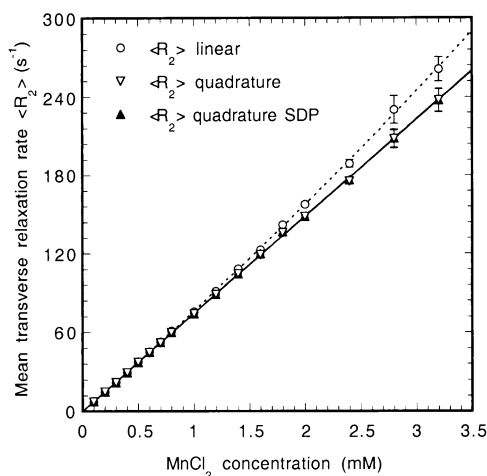
Fig. 3. $\langle R_2 \rangle$ versus $MnCl_2$ concentration for the homogeneous $MnCl_2$ phantoms. The three data sets are for analysis with quadrature and linear subtraction of the signal level offset, as well as quadrature subtraction analysis with spin density projection (SDP). The $\langle R_2 \rangle$ values for the quadrature subtraction analysis are linearly correlated with $MnCl_2$ concentration ($r = 0.99991$). The error bars show the standard deviation on R_2. The solid line is a linear fit, and the dashed line a quadratic fit.

compared with 73% for the analysis without spin density projection.

3.3. Heterogenous system

3.3.1. Mono-exponential R_2 analysis

The results of the mono-exponential transverse relaxation rate analysis of the dual compartment $MnCl_2$ phantom system are shown in Fig. 4 with $\langle R_2 \rangle$ plotted versus $MnCl_2$
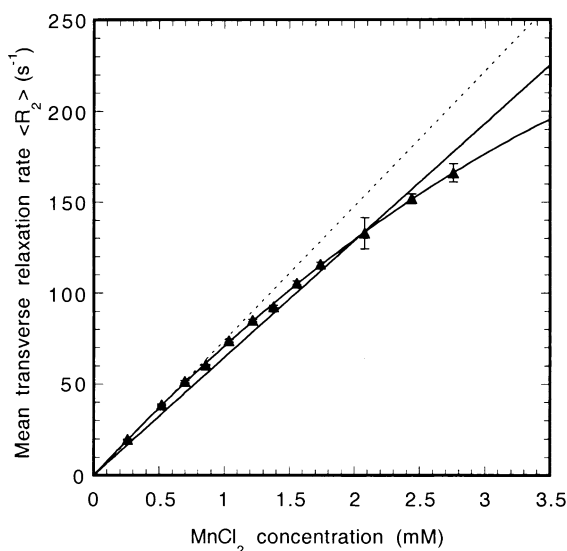

Fig. 4. $\langle R_2 \rangle$ versus $MnCl_2$ concentration for mono-exponential analysis of the simulated dual compartment $MnCl_2$ phantom system. The solid lines show a linear and quadratic fit to the data. The dashed line represents a relaxivity of 74.3 s^{-1} mM^{-1}, as determined from the homogeneous $MnCl_2$ phantoms. The error bars show the standard deviation on R_2.

concentration. An F-test on the reduced χ-squares ratio between a linear and quadratic fit to the $\langle R_2 \rangle$ versus $[MnCl_2]$ data indicates that the quadratic is a statistically better fit to the data, with a significance level $p < 0.01$. This demonstrates that mono-exponential R_2 analysis of dual compartment transverse relaxation systems results in a non-linear relationship between the average R_2 value and paramagnetic ion concentration. However, it is relevant to note that the linear term of the quadratic equates to a relaxivity value of 75.9 ± 1.4 s^{-1} mM^{-1}, which is comparable to that for the homogeneous $MnCl_2$ phantom system.

3.3.2. Bi-exponential R_2 analysis

The average transverse relaxation rate from bi-exponential R_2 image analysis of the dual compartment $MnCl_2$ phantom system is plotted in Fig. 5 versus the effective $MnCl_2$ concentration. Fig. 5a shows the $\langle R_2 \rangle$ result for quadrature subtraction analysis incorporating spin density projection, while Fig. 5b shows the result for R_2 analysis performed without spin density projection. There is a highly significant linear correlation between $\langle R_2 \rangle$ and $[MnCl_2]$ for each analysis, with a linear fit yielding a relaxivity comparable to that for mono-exponential analysis of the homogeneous phantom system (dashed line). The relaxivity for the analysis with spin density projection was 77.5 ± 0.8 s^{-1} mM^{-1}, while the relaxivity for the analysis without spin density projection was 72.5 ± 1.0 s^{-1} mM^{-1}. The χ-squares probability for the goodness-of-fit for the two analyses satisfied the criterion $\chi^2 \leq \nu$ for an acceptable fit to the data for all of the phantoms. The bi-exponential R_2 analysis with spin density projection was better than the analysis without, for which the minimum Q_χ was 64%, as compared to 53% for the analysis without spin density projection.

The transverse relaxation components of the dual compartment $MnCl_2$ phantom system derived from bi-exponential R_2 image analysis with quadrature subtraction of the signal level offset are shown in Fig. 6. The fast R_2 component of the higher $MnCl_2$ concentration compartment, for analysis with and without spin density projection, is shown in Figs. 6a and 6b, respectively. The relaxivity for the fast relaxation component was 75.8 ± 1.7 s^{-1} mM^{-1} for analysis with spin density projection (Fig. 6a), and 67.1 ± 1.3 s^{-1} mM^{-1} for the analysis without spin density projection (Fig. 6b). Figs. 6c and 6d show the slow transverse relaxation rate component for the lower $MnCl_2$ concentration compartment. With spin density projection, the relaxivity for the slow relaxation component (Fig. 6c) was 72.9 ± 2.5 s^{-1} mM^{-1}. For the bi-exponential analysis without spin density projection (Fig. 6d), there was no significant correlation between the $\langle R_{2s} \rangle$ and $[MnCl_2]$ data for a linear fit. The relative spin population density of the fast relaxation component for each phantom, plotted against the $MnCl_2$ concentration of the higher concentration compartment, is shown in Figs. 6e and 6f for analysis with and without spin density projection, respectively. The mean population den-
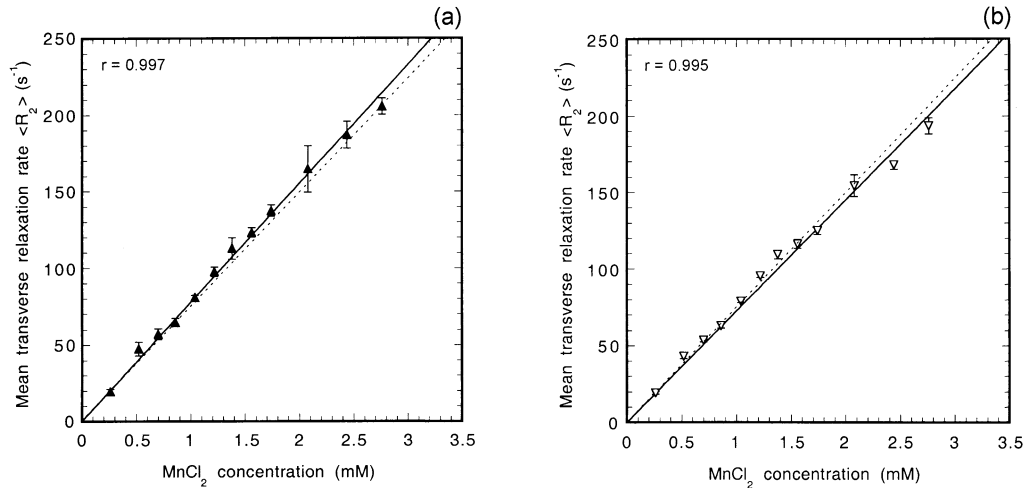
Fig. 5. The average $\langle R_2 \rangle$ value versus $MnCl_2$ concentration for bi-exponential analysis of the simulated dual compartment $MnCl_2$ phantom system, with and without spin density projection ((a) and (b), respectively). The dashed line represents a relaxivity of 74.3 s^{-1} mM^{-1}. The solid lines are linear fits to the data. The error bars show the standard deviation on R_2.

sity of the fast relaxation component for the entire set of phantoms was $80 \pm 7\%$ for the spin density projection analysis, and $89 \pm 6\%$ for the analysis without spin density projection (cf. actual population density for the faster relaxing component of 85%). For average $\langle R_2 \rangle$ values greater than 100 s^{-1}, bi-exponential R_2 analysis with spin density projection provides more accurate measurement of the relative population densities than the analysis without spin density projection ($\rho_f = 83 \pm 5\%$ and $93 \pm 3\%$, respectively). An *F*-test on the reduced χ-squares ratio for accepting the additional exponential term in bi-exponential R_2 image analysis of the dual compartment $MnCl_2$ phantom system, indicated that bi-exponential R_2 analysis with spin density projection was statistically better than mono-exponential analysis for average $\langle R_2 \rangle$ values greater than 100 s^{-1}, for which the reduced χ^2 ratio probability was (on average) greater than 95% ($p < 0.05$).

4. Discussion

The accurate quantification of proton transverse relaxation processes in systems where there is compartmentalisation of the transverse relaxation requires multi-exponential analysis of the transverse magnetisation decay. For example, bi-exponential modeling of transverse relaxation in tissues has been shown to distinguish between the chemical compartmentalisation of hydrogen protons, such as that between water and fat [27–29], as well as that of different anatomic compartments, such as intracellular and extracellular water [13,16,30,31], and the free and bound water of proteins [32–34]. The extent to which particular compartments dominate the observed relaxation behavior depends on their relative population densities, the span of measurement times, and on whether the echo times accommodate

the slow exchange of hydrogen protons between anatomic compartments over the time course of the spin-echo measurement. When two particular compartments dominate the transverse relaxation process, bi-exponential analysis not only provides the facility to distinguish between these compartments, but also provides greater accuracy in determining the overall average relaxation rate of the system. Bi-exponential analysis can also distinguish partial volume effects where these dominate the observed relaxation behavior, such as that between cerebrospinal fluid and brain tissue [35–37].

In the context of liver iron overload, bi-exponential transverse relaxation rate analysis has been shown to discriminate between the intracellular and extracellular water of the liver in iron loaded marmosets [16]. This compartmentalisation has also been reported in muscle tissue [13], where bi-exponential relaxation reverted to mono-exponential relaxation after maceration of the sample and the subsequent destruction of cell boundaries. This may explain the linear correlation observed between single exponential R_2 values and liver iron concentration in iron loaded autopsy liver tissue [11], given autolysis of the liver cells [38].

4.1. Bi-exponential proton transverse relaxation rate analysis

To accurately quantify bi-exponential transverse relaxation processes where a small number of images are available for analysis, particular care must be taken in the choice of the curve-fitting algorithm used for calculating the components of the transverse magnetisation decay. Non-linear least squares (χ^2) minimization by means of the Levenberg-Marquadt method [20,21] was inadequate to this task. This method has difficulty in converging to the correct numerical solution when there is a complicated topography to the χ^2
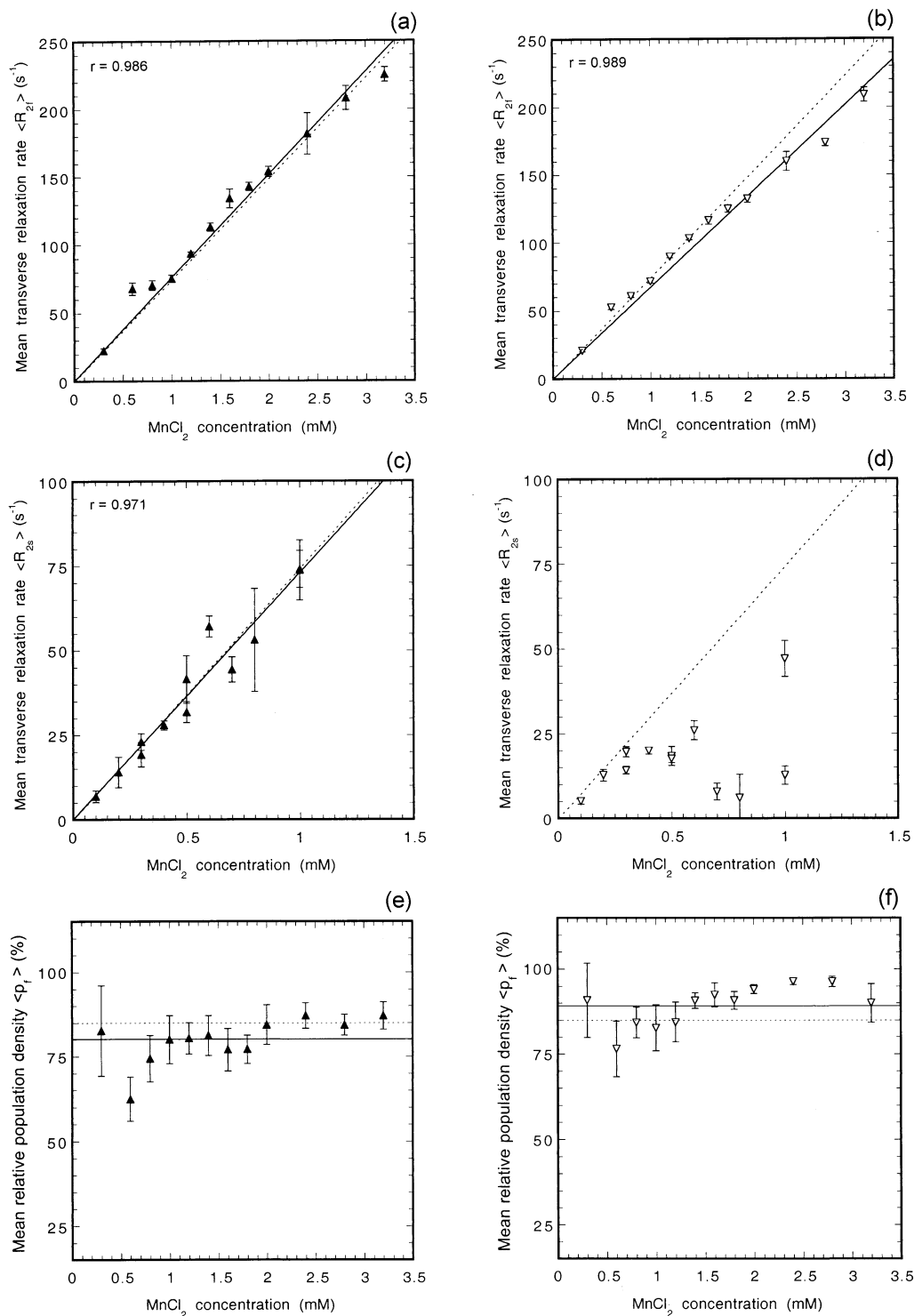
Fig. 6. The individual components for bi-exponential analysis of the simulated dual compartment $MnCl_2$ phantom system, with and without spin density projection (solid and open triangles, respectively). (a, b) $\langle R_{2f} \rangle$ versus $MnCl_2$ concentration. (c, d) $\langle R_{2s} \rangle$ versus $MnCl_2$ concentration. The solid line is a linear fit. The dashed line represents a relaxivity of 74.3 s^{-1} mM^{-1}. (e, f) $\langle \rho_f \rangle$ versus $MnCl_2$ concentration. The solid line is the mean of $\langle \rho_f \rangle$, the dashed line is the expected 85% value. Error bars show the standard deviation of each component.

hyper-surface of possible solutions in the vicinity of the optimal solution [21]. Near-degeneracy around the optimal solution is typical when fitting a model that is a summation of identical terms—such as multiple exponentials—partic-

ularly where the measurement errors are large or the data set is small. To improve the sensitivity of curve fitting to the bi-exponential components, a minimization strategy was developed based on the simplex-simulated annealing

method of Press and Teukolsky [23], with the ability to handle parameter constraints. Simplex-simulated annealing procedures are more sensitive to the topography of the hyper-surface of possible solutions than direct search methods. The objective function to be minimized was constructed around a least-pth formulation [25,26] of the difference between the fitted model and the measured data, relative to the uncertainty on the measurements. This formulation of the objective function provided greater resolution of the hyper-surface of possible solutions and represents a χ-pth minimization as opposed to χ^2 minimization procedure.

In addition to the choice of curve fitting algorithm, particular attention must be paid to the signal-to-noise level to accurately quantify the bi-exponential transverse relaxation components. Where the signal-to-noise ratio is low (SNR $\leq$ 3), it is important to accurately model the underlying noise distribution of the magnitude MR images, and to appropriately correct for the signal level offset [19]. Also, where the transverse relaxation times are shorter than the minimum echo time, the curve fitting will need to be weighted toward an estimate of the initial signal intensity to achieve sufficient accuracy in discrimination of the bi-exponential components, as has been demonstrated in the present study.

4.2. Noise distribution modeling

Transverse relaxation parameters are typically determined from magnitude MR data for which there is a non-zero baseline in signal intensity. This baseline arises owing to the presence of noise in both the real and imaginary components of the complex MR signal, which is acquired by quadrature detection. Where the noise in the detection channels is Gaussian distributed (as for thermal noise), a Rician noise distribution will be generated in the magnitude data with non-zero mean, resulting in a signal level offset in the magnitude image [19].

Although the thermal noise in magnitude MR data is Rician distributed, and can be shown to follow the Rayleigh distribution when no object is present [19], other sources of noise may be perturb this behavior. Gudbjartsson and Patz [19] reported that the expected Rayleigh noise distribution for magnitude MR data could not be statistically verified for an image comprised only of noise and without any phase artifacts. This may be a consequence of non-random sources of noise in the imaging process, such as that due to drift in magnetic induction, or nonuniform signal distributions [18]. Further, in the presence of a patient, structured noise will arise due to respiratory motion, such as ghosting, and mottling in the phase-encoding direction [39].

These additional sources of noise may lead to over-dispersion of the Rician distributed thermal noise component. In this study, a generalized Poisson distribution (GPD) [17] was found to give a statistically better fit to the background noise than the Rician distribution ($p < 0.05$). The

GPD includes a dispersive term λ, which helps account for the additional noise components.

4.3. Baseline correction

To accurately quantify transverse relaxation processes at low signal-to-noise ratios (SNR $\leq$ 3), the non-zero baseline in the magnitude MR data must be subtracted in quadrature from the image intensities. The basis of this correction scheme may be explained with regard to the origin of the measured complex signal ($\boldsymbol{M}$), which is the combined signal from the actual signal ($\boldsymbol{A} = A \angle \theta$) and a random noise component ($\boldsymbol{\sigma} = \sigma \angle \phi$) in the complex plane. The squared magnitude of M is given by the expression

$$M^2 = A^2 + \sigma^2 + 2A\sigma \cos(\theta - \phi)$$

where $M = |\boldsymbol{M}|$, $A = |\boldsymbol{A}|$, $\sigma = |\boldsymbol{\sigma}|$, and θ-ϕ is the angle between the complex vectors $\boldsymbol{A}$ and $\boldsymbol{\sigma}$. As the magnitude image is the result of many separate measurements, the cross component will average to zero given the random orientation of the noise component. A random process also governs the magnitude of the noise component, but over many separate measurements, the magnitude tends toward an average value. The actual signal from the object in the absence of noise may then be simply calculated as

$$A_i = \sqrt{M_i^2 - \sigma_i^2}$$

where A_i is the actual signal for the object in the image, M_i is the measured signal from the object in the image, and σ_i is the mean (magnitude) of the background noise in the image.

Previous studies of liver iron overload that have investigated the correlation between R_2 and liver iron concentration have either ignored the signal level offset in the magnitude image data [4], or employed linear subtraction of the signal level offset [10,11], or modeling of the offset by an additive baseline [5]. However, with diminishing signal-to-noise, linear subtraction of the signal level offset increasingly overestimates the actual transverse relaxation rate, as has been shown for the homogeneous $MnCl_2$ phantom system in the present study. For the 2.8 and 3.2 mM $MnCl_2$ solutions, where the SNR was less than 2 in the longest echo time image, R_2 image analysis with linear subtraction of the signal level offset overestimated R_2 by more than 10%. The increasing overestimation of R_2 with loss in phantom signal intensity results in a quadratic trend to the $\langle R_2 \rangle$ versus $[MnCl_2]$ data, with a statistically significant deviation from the expected linear relationship between R_2 and paramagnetic ion concentration in solution ($p < 0.01$, F-test). In contrast, for the R_2 image analysis with quadrature subtraction of the signal level offset, there was a highly significant linear correlation between $\langle R_2 \rangle$ and $[MnCl_2]$. The relaxivity value of $74.3 \pm 0.2 \text{ s}^{-1} \text{ mM}^{-1}$ for the linear fit to the data are in close agreement with that determined from other spin-echo image measurements of $MnCl_2$ phantoms [40],

for which the relaxivity value was calculated as 74.0 s^{-1} mM^{-1} at a temperature of 20°C.

4.4. Spin density projection

The method of RF field intensity-weighted spin density projection outlined in the present study is applicable to axial MR images acquired with a chest coil, where the region of interest under study is surrounded by an essentially homogeneous medium for which there has been negligible decay in signal intensity at the minimum image acquisition time. For R$_2$ measurements of liver iron overload utilizing echo times of 6 to 18 ms [10], a suitable medium would be that provided by the subcutaneous (s.c.) fat surrounding the abdomen of the patient. With reference to the relative spin densities between the s.c. fat and liver tissue, an estimate of the initial signal within the liver may potentially be obtained.

In the present study, a suitable medium for spin density projection was provided by bags of lard positioned around the MnCl$_2$ phantoms. When the projected spin densities for the MnCl$_2$ phantoms were incorporated into the mono-exponential R$_2$ image analysis of the homogeneous phantom system (with quadrature subtraction of the signal level offset), no statistically significant difference was found between the R$_2$ data calculated with or without spin density projection. This result indicates that there is no bias to the inclusion of RF field intensity-weighted spin densities in the R$_2$ image analysis methodology. The R$_2$ image analysis with spin density projection actually provided a statistically better fit to the signal intensity data than the analysis without spin density projection, as determined by the χ-squares test.

4.5. Mono-exponential analysis of dual R$_2$ systems

When mono-exponential transverse relaxation rate analysis is performed on the bi-exponential MnCl$_2$ phantom system, there is a significant deviation from the expected linear relationship between measured $\langle R_2 \rangle$ and [MnCl$_2$]. A second order polynomial provides a statistically better fit to the data than linear regression ($p < 0.01$, F-test). Mono-exponential analysis increasingly underestimates the average transverse relaxation rate as the concentration of paramagnetic ions increases, and for compartmentalised proton densities in relative percentages of 85% and 15%, the error on the expected average R$_2$ value is greater than 10% for expected average R$_2$ values greater than 95 s^{-1} (i.e., transverse relaxation times less than 11 ms).

4.6. Bi-exponential analysis of dual R$_2$ systems

The bi-exponential R$_2$ analysis of the simulated dual compartment MnCl$_2$ phantom system with quadrature subtraction of the signal level offset satisfied the criterion for an acceptable fit to the spin-echo image data for all of the phantoms, with $\chi^2 \leq \nu$. However, the R$_2$ analysis without spin density projection was unable to resolve the bi-exponential components to sufficient accuracy for average relaxation rates in excess of 100 s^{-1}. The measured relative population density of the fast relaxation component ρ_f for R_{2f} values greater than 100 s^{-1} was on average 93%, as opposed to 83% for the analysis with spin density projection. This overestimate of ρ_f, while only a 10% increase over the actual value of 85%, equates to an underestimation of the population density of the slow relaxation component ρ_s of 53%. As a consequence, the quantification of the slow relaxation rate becomes extremely problematical, as shown in Fig. 6d. This is in marked contrast to the analysis performed with spin density projection, for which the slow transverse relaxation rate correlated with the MnCl$_2$ concentration of the 15% by volume compartment with a Pearson's correlation coefficient of 0.97. The relaxivities for the fast and slow relaxation compartments of the aqueous MnCl$_2$ for the analysis with spin density projection were 75.8 ± 1.7 s^{-1} mM^{-1} and 72.9 ± 2.5 s^{-1} mM^{-1} respectively, which is in agreement with the homogeneous MnCl$_2$ phantom relaxivity of 74.3 ± 0.2 s^{-1} mM^{-1}, within measurement uncertainties.

5. Conclusion

The bi-exponential proton transverse relaxation rate image analysis technique presented in this study is particularly well suited to the discrimination of dual compartment transverse relaxation behavior where a limited number of spin-echo images are available for analysis. Further, the method of RF field intensity-weighted spin density projection enables the accurate determination of bi-exponential components in instances of rapid transverse relaxation enhancement, where the transverse relaxation rate is shorter than the minimum echo time available for measurement. In summary of the efficacy of R$_2$ image analysis with RF field intensity-weighted spin density projection, it has been demonstrated that:

i) spin density projection does not introduce any bias into the mono-exponential analysis,
ii) the bi-exponential analysis reliably quantifies both the fast and slow relaxation components,
iii) bi-exponential analysis is statistically better than mono-exponential analysis in dual compartment transverse relaxation systems for average relaxation rates higher than 100 s^{-1}.

The bi-exponential R$_2$ image analysis technique presented in this study may thus have direct application to the measurement and mapping of liver iron concentrations [3–5,10], which involves the measurement of R$_2$ values ranging from those found in normal hepatic tissue to those in excess of 200 s^{-1}, as found in heavily iron loaded patients [9].

Acknowledgments

Appendix

To determine whether one model for a given set of data was better than another model, the F-test on the reduced χ-squares ratio was used [41]:

$$F = \frac{\chi_1^2 / \nu_1}{\chi_2^2 / \nu_2}$$

where ν_1 and ν_2 are the number of degrees of freedom corresponding to χ_1^2 and χ_2^2. One model can be statistically rejected over another if the reduced χ-squares ratio exceeds a threshold value for the given significance level, e.g., $p < 0.05$. The model to be rejected will have a reduced χ^2 (χ^2/ν) greater than that for the more appropriate model. The significance level p to which a given model is better than another model may be determined from the F statistic by the incomplete beta function [21]

$$Q_F(F; \nu_1, \nu_2) = I_{\nu_2/\nu_2 + \nu_1 F}\left(\frac{\nu_2}{2}, \frac{\nu_1}{2}\right)$$

where

$$I_x(a, b) = \frac{\Gamma(a + b)}{\Gamma(a)\Gamma(b)} \int_0^x t^{a-1}(1 - t)^{b-1} \, dt$$

and $\Gamma(z)$ is the gamma function. This may be expressed as the percentage probability with which the given model is better than the alternative model by

$$P_F(F) = 100(1 - Q_F(F)).$$

However, when the probability $P_F(F)$ is less than that for the desired significance level (e.g., $p = 0.05$ or $P_F(F) = 95\%$) this is not to say that the proposed model is incorrect, but only that the validity of the proposed model over the alternative model cannot be statistically verified [41]. It is only where $P_F(F) < 5\%$ that we state that the alternative model is statistically better than the proposed model.

To determine whether a bi-exponential fit to the image data was better (in a statistical sense) than the mono-exponential fit, a variant of the reduced χ-squares ratio was used to determine whether there was any statistical improvement in adding the extra exponential term. According to Bevington [41], the appropriate figure of merit for evaluating the statistical significance of the model with the additional term is the difference of the χ^2 values for the two models, divided by the reduced χ^2 value of the expanded model. This ratio is then a measure of how much the additional term has

improved the reduced χ^2. The test statistic F for accepting the bi-exponential model over the mono-exponential model is

$$F = \frac{(\chi_b^2 - \chi_m^2)/(\nu_b - \nu_m)}{\chi_b^2/\nu_b}$$

where ν_b and ν_m are the number of degrees of freedom corresponding to χ_b^2 and χ_m^2 for the bi-exponential model and mono-exponential model, respectively. The significance level p is given by the incomplete beta function above where $\nu_1 = \nu_b - \nu_m$ and $\nu_2 = \nu_b$.

The F-test is a more suitable statistic than the χ^2 test in determining the validity of a given model over another, as the χ^2 test is not only sensitive to the discrepancies between the fitted model and the data, but also to the uncertainties on the data, which may not be satisfactorily known [41]. This situation arose in determination of the underlying noise distribution of the image data from the background noise. For the phantom data, the χ^2 test *could be used* to determine the goodness-of-fit of either the mono-exponential fit or bi-exponential fit in the R_2 image analysis, given the suitable estimation of the uncertainties on the data. The χ^2 probability that the resulting fit was the best fit to the data (for the specified model) was determined via the χ^2 probability relationship to the incomplete gamma function [21]

$$Q_\chi(\chi^2; \nu) = Q\left(\frac{\nu}{2}, \frac{\chi^2}{2}\right)$$

where

$$Q(a, x) = \frac{1}{\Gamma(a)} \int_x^\infty e^{-t} t^{a-1} dt, \, a > 0.$$

A "moderately" good fit is often quoted for instances where $\chi^2 \leq \nu$ [21], equivalent to Q_χ exceeding approximately 50% (for $\nu \leq 30$).

References

[1] Jensen PD, Jensen FT, Christensen T, Ellegaard J. Non-invasive assessment of tissue iron overload in the liver by magnetic resonance imaging. Br J Radiol 1994;87(1):171–84.

[2] Bonkovsky HL, Rubin RB, Cable EE, Davidoff A, Rijcken TH, Stark DD. Hepatic iron concentration: noninvasive estimation by means of MR imaging techniques. Radiology 1999;212(1):227–34.

[3] Kaltwasser JP, Gottschalk R, Schalk KP, Hartl W. Non-invasive quantitation of liver iron-overload by magnetic resonance imaging. Br J Haematol 1990;74(3):360–3.

[4] Engelhardt R, Langkowski JH, Fischer R, Nielsen P, Kooijman H, Heinrich HC, Bucheler E. Liver iron quantification: studies in aqueous iron solutions, iron overloaded rats, and patients with hereditary hemochromatosis. Magn Reson Imaging 1994;12(7):999–1007.

[5] Papakonstantinou OG, Maris TG, Kostaridou V, Gouliamos AD, Koutoulas GK, Kalovidouris AE, Papavassiliou GB, Kordas G, Kattamis C, Vlahos LJ, et al. Assessment of liver iron overload by T2-quantitative magnetic resonance imaging: correlation of T2-QMRI measurements with serum ferritin concentration and histologic grading of siderosis. Magn Reson Imaging 1995;13(7):967–77.

[6] Brown DW, Henkelman RM, Poon PY, Fisher MM. Nuclear magnetic resonance study of iron overload in liver tissue. Magn Reson Imaging 1985;3(3):275–82.

[7] Hernandez RJ, Sarnaik SA, Lande I, Aisen AM, Glazer GM, Chenevert T, Martel W. MR evaluation of liver iron overload. J Comput Assist Tomogr 1988;12(1):91–4.

[8] Dixon RM, Styles P, al-Refaie FN, Kemp GJ, Donohue SM, Wonke B, Hoffbrand AV, Radda GK, Rajagopalan B. Assessment of hepatic iron overload in thalassemic patients by magnetic resonance spectroscopy. Hepatology 1994;19(4):904–10.

[9] Wang ZYJ, Haselgrove JC, Martin MB, Hubbard AM, Li SC, Loomes K, Moore JR, Zhao HQ, Cohen AR. Evaluation of iron overload by single voxel MRS measurement of liver T2. JMRI 2002; 15(4):395–400.

[10] Clark PR, St Pierre TG. Quantitative mapping of transverse relaxivity ($1/T_2$) in hepatic iron overload: a single spin-echo imaging methodology. Magn Reson Imaging 2000;18(4):431–8.

[11] Clark PR, Chua-anusorn W, St Pierre TG. Proton transverse relaxation rate (R_2) images of liver tissue: mapping local tissue iron concentrations with MRI. Magn Reson Med 2002;49(3):572–5.

[12] Brix G, Schad LR, Lorenz WJ. Evaluation of proton density by magnetic resonance imaging: phantom experiments and analysis of multiple component proton transverse relaxation. Phys Med Biol 1990;35(1):53–66.

[13] Cole W, LeBlanc A, Jhingran S. The origin of biexponential T_2 relaxation in muscle water. Magn Reson Imaging 1993;29(1):19–24.

[14] Thomsen C, Wiggers P, Ring-Larsen H, Christiansen E, Dalhoj J, Henriksen O, Christoffersen P. Identification of patients with hereditary haemochromatosis by magnetic resonance imaging and spectroscopic relaxation time measurements. Magn Reson Imaging 1992; 10(6):867–79.

[15] Barthwal R, Hohn-Berlage M, Gersonde K. In vitro proton T1 and T2 studies on rat liver: analysis of multiexponential relaxation processes. Magn Reson Med 1986;3(6):863–75.

[16] Bulte JWM, Miller GF, Vymazal J, Brooks RA, Frank JA. Hepatic hemosiderosis in non-human primates—quantification of liver iron using different field strengths. Magn Reson Med 1997;37(4):530–6.

[17] Consul PC. Generalized Poisson distributions: properties and applications. In: Owen DB, editor. Statistics: textbooks and monographs, Vol. 99. New York: Marcel Dekker, 1989.

[18] Sijbers J. Signal and noise estimation from magnetic resonance images, PhD Thesis. 1998, University of Antwerp.

[19] Gudbjartsson H, Patz S. The Rician distribution of noisy MRI data. Magn Reson Med 1995;34(6):910–4.

[20] Marquardt DW. An algorithm for least-squares estimation of non-linear parameters. J Soc Indust Appl Math 1963;11:431–41.

[21] Press WH, Teukolsky SA, Vetterling WT, Flannery BP. Numerical recipes in C: the art of scientific computing. Cambridge: Cambridge University Press, 1992.

[22] Andersen AH. On the Rician distribution of noisy MRI data. Magn Reson Med 1996;36(2):331–3.

[23] Press WH, Teukolsky SA. Simulated annealing optimization over continuous spaces. Comput Phys 1991;5(4):426–9.

[24] Hendrick RE. Image contrast and noise. In: Stark DD, Bradley WG, editors. Magnetic Resonance Imaging. St. Louis: The C. V. Mosby Company, 1988. p. 67–72.

[25] Temes GC, Zai DYF. Least pth approximation. IEEE Trans CT 1969;16(2):235–7.

[26] Charalambous C, Bandler JW. New algorithms for network optimization. IEEE Trans MTT 1973;21(12):815–8.

[27] Kamman RL, Go KG, Muskiet FA, Stomp GP, Van Dijk P, Berendsen HJ. Proton spin relaxation studies of fatty tissue and cerebral white matter. Magn Reson Imaging 1984;2(3):211–20.

[28] Kamman RL, Bakker CJ, van Dijk P, Stomp GP, Heiner AP, Berendsen HJ. Multiexponential relaxation analysis with MR imaging and NMR spectroscopy using fat-water systems. Magn Reson Imaging 1987;5(5):381–92.

[29] Brix G, Heiland S, Bellemann M, Kock T, Lorenz W. MR imaging of fat-containing tissues: valuation of two quantitative imaging techniques in comparison with localised proton spectroscopy. Magn Reson Imaging 1993;11:977–91.

[30] Jouvensal L, Carlier P, Bloch G. Evidence for bi-exponential transverse relaxation of lactate in excised rat muscle. Magn Reson Med 1999;41:624–6.

[31] Beaulieu C, Fenrich F, Allen P. Multicomponent water proton transverse relaxation and T2-discriminated water diffusion in myelinated and nonmyelinated nerve. Magn Reson Imaging 1998;16(10):1201–10.

[32] Moser E, Holzmueller P, Krssak M. Improved estimation of tissue hydration and bound water fraction in rat liver tissue. MAGMA 1996;4(1):55–9.

[33] Burtea C, Gatina R, Stoian G, Mardare M, Dumitru IF, Dragomir CT. Spin-spin relaxation times in myocardial hypertrophy induced by endocrine agents in rat. MAGMA 1998;7(3):184–98.

[34] Stankeiwicz PJ, Metz KR, Sassani JW, Briggs RW. Nuclear magnetic resonance study of free and bound water fractions in normal lenses. Invest Ophthalmol Vis Sci 1989;30(11):2361–9.

[35] Schad LR, Brix G, Zuna I, Harle W, Lorenz WJ, Semmler W. Multiexponential proton spin-spin relaxation in MR imaging of human brain tumors. J Comput Assist Tomogr 1989;13(4):577–87.

[36] Cheng KH. In vivo characterization of human brain by chisquares parameter maps: multiparameter proton T2-relaxation analysis. Magn Reson Imaging 1994;12(7):1099–109.

[37] Whittall K, MacKay A, Li D. Are mono-exponential fits to a few echoes sufficient to determine T2 relaxation in vivo human brain? Magn Reson Med 1999;41(6):1255–7.

[38] Gallagher C, Judah J, Rees K. Enzyme changes during liver autolysis. J Path Bact 1956;72:247–55.

[39] Bellon EM, Haacke EM, Coleman PE, Sacco DC, Steiger DA, Gangarosa RE. MR artifacts: a review. AJR 1986;147(6):1271–81.

[40] Andersen C, Jensen FT. Precision, accuracy, and image plane uniformity in NMR relaxation time imaging on a 1.5 T whole-body MR imaging system. Magn Reson Imaging 1994;12(5):775–84.

[41] Bevington PR, Kieth Robinson D. Data reduction and error analysis for the physical sciences. New York: McGraw-Hill, Inc., 1992.